Hornsen Tzou[1]
State Key Laboratory of Mechanics and Control of Mechanical Structures,
Interdisciplinary Research Institute of Aeronautics and Astronautics,
College of Aerospace Engineering,
Nanjing University of Aeronautics and Astronautics,
Nanjing 210016, China
e-mail: hstzou@nuaa.edu.cn

Bolei Deng
StrucTronics and Control Laboratory,
School of Aeronautics and Astronautics,
Zhejiang University,
Hangzhou 310027, China

Huiyu Li
The State Key Laboratory of Fluid Power Transmission and Control,
School of Mechanical Engineering,
Zhejiang University,
Hangzhou 310027, China

Flexoelectric Actuation and Vibration Control of Ring Shells

The converse flexoelectric effect, i.e., the polarization (or electric field) gradient-induced internal stress (or strain), can be utilized to actuate and control flexible structures. This study focuses on the microscopic actuation behavior and effectiveness of a flexoelectric actuator patch laminated on an elastic ring shell. An atomic force microscope (AFM) probe is placed on the upper surface of the flexoelectric patch to induce an inhomogeneous electric field resulting in internal stresses of the actuator patch. The flexoelectric stress-induced membrane control force and bending control moment regulate the ring vibration and their actuation mechanics, i.e., transverse and circumferential control actions, are, respectively, studied. For the transverse direction, the electric field gradient quickly decays along the ring thickness, resulting in a nonuniform transverse distribution of the induced stress, and this distribution profile is not influenced by the actuator thickness. The flexoelectric-induced circumferential membrane control force and bending control moment resemble the Dirac delta functions at the AFM contact point. The flexoelectric actuation can be regarded as a localized drastic bending to the ring. To evaluate the actuation effect, dynamic responses and controllable displacements of the elastic ring with flexoelectric actuations are analyzed with respect to design parameters, such as the flexoelectric patch thickness, AFM probe radius, ring thickness, and ring radius.
[DOI: 10.1115/1.4036097]

Introduction

Precision actuation and vibration control are essential in many engineering applications. This study is to evaluate precision flexoelectric actuation and control of ring structures. The electromechanical coupling that the polarization (or electric field) gradient inducing internal stress (or strain) is called the *converse flexoelectric effect* [1–3]. In the last decade, both theoretical estimations [4–6] and experimental measurements of flexoelectric coefficients [7,8] of various materials [9–11] were carried out. Signal analysis and energy generation of flexoelectric materials were recently evaluated and their applications on rings and cylindrical shells were studied [12–15]. These studies presented a new flexoelectric sensing and energy generation mechanism, as compared with the conventional piezoelectric sensing/energy harvesting technique. Static flexoelectric actuation effects of a cantilever beam using an atomic force microscope (AFM) probe were also evaluated [16]. This study focuses on flexoelectric dynamic actuation and vibration control of ring shells.

Ring-type structures are widely used in engineering applications, such as gears, motors, stiffeners, etc. Natural frequencies and mode shapes of free-floating rings have been thoroughly studied [17]. Piezoelectric sensors and actuators and their orthogonal modal sensing and actuation effects of rings were analyzed [18,19]. However, flexoelectric dynamic actuation characteristics and vibration control of shell structures have not been evaluated previously. Thus, this study is to investigate flexoelectric microscopic actuation and control behaviors of ring structures. An inhomogeneous electric field generated by an AFM probe is used to actuate a flexoelectric patch laminated on the ring structure. With the flexoelectric membrane control force and bending control moment, steady-state dynamic responses and controllable displacements of the ring are determined. Distribution of the electric field gradient over the transverse direction of different patch thickness is analyzed, followed by actuation effectiveness of the actuator thickness, AFM probe radius, ring thickness, and ring radius. The objective focuses on the flexoelectric actuator's microscopic behavior, i.e., the flexoelectric actuation mechanism with an AFM probe is thoroughly evaluated. Furthermore, the extremely inhomogeneous AFM probe's electric field and the drastic "buckling" behavior induced by the flexoelectric actuator are investigated.

Ring Dynamics

Figure 1 illustrates an elastic ring shell laminated with a flexoelectric actuator patch, where α_3 and ψ, respectively, define the transverse and the circumferential directions; R is the neutral surface radius of the ring; h is the ring thickness, and b is the ring width.

The flexoelectric actuator patch is much thinner than the ring, and thus, its stiffness/mass effect to the ring dynamics is neglected. Only the induced flexoelectric membrane control force $N^a_{\psi\psi}$ and bending control moment $M^a_{\psi\psi}$ (where a denotes the actuator-induced component) are considered in the system dynamics. Dynamic equations of the ring with mechanical and actuation forces can be simplified from the dynamic equations of the double-curvature shell [20]

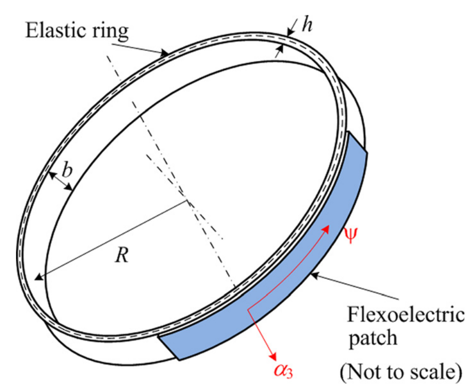

Fig. 1 Schematic diagram of the elastic ring

[1]Corresponding author.

Contributed by the Technical Committee on Vibration and Sound of ASME for publication in the JOURNAL OF VIBRATION AND ACOUSTICS. Manuscript received May 31, 2015; final manuscript received January 10, 2017; published online April 24, 2017. Editor: I. Y. (Steve) Shen.

$$\rho h\frac{\partial^2 u_\psi}{\partial t^2}-\frac{1}{R}\frac{\partial N^m_{\psi\psi}}{\partial\psi}-\frac{1}{R^2}\frac{\partial M^m_{\psi\psi}}{\partial\psi}=-\frac{1}{R}\frac{\partial N^a_{\psi\psi}}{\partial\psi}-\frac{1}{R^2}\frac{\partial M^a_{\psi\psi}}{\partial\psi} \quad (1a)$$

$$\rho h\frac{\partial^2 u_3}{\partial t^2}+\frac{N^m_{\psi\psi}}{R}-\frac{1}{R^2}\frac{\partial^2 M^m_{\psi\psi}}{\partial\psi^2}=\frac{N^a_{\psi\psi}}{R}-\frac{1}{R^2}\frac{\partial^2 M^a_{\psi\psi}}{\partial\psi^2}+F_3 \quad (1b)$$

where ρ is ring's mass-density; h is the ring thickness; u_3 is the transverse displacement; u_ψ is the circumferential displacement, which is assumed small as compared with u_3; F_3 is the transverse distributed mechanical force; and $N^m_{\psi\psi}$ and $M^m_{\psi\psi}$ are, respectively, the elastic membrane force and bending moment per unit width, where the superscript m denotes the mechanical component. Note that the circumferential and transverse motions are coupled and usually the transverse oscillation dominates. Combining the actuator-induced components in ring equations, Love's control operators [20] of the flexoelectric laminated ring can be expressed as

$$L^a_\psi=-\frac{1}{R}\frac{\partial N^a_{\psi\psi}}{\partial\psi}-\frac{1}{R^2}\frac{\partial M^a_{\psi\psi}}{\partial\psi} \quad (2a)$$

$$L^a_3=\frac{N^a_{\psi\psi}}{R}-\frac{1}{R^2}\frac{\partial^2 M^a_{\psi\psi}}{\partial\psi^2} \quad (2b)$$

where L^a_ψ and L^a_3 are Love's actuation or control operators induced by the flexoelectric actuators, respectively, in the circumferential and transverse directions. Periodical boundary conditions are required for the ring shells, i.e., $u_\psi(\psi+2\pi)=u_\psi(\psi)$ and $u_3(\psi+2\pi)=u_3(\psi)$. With the modal expansion method, ring's dynamic displacements can be expressed by adding all participating natural modes multiplied by their respective modal participation factors [17,20]

$$u_\psi(\psi,t)=\sum_{k=2}^{\infty}\eta_k(t)U_{\psi k}(\psi,t) \quad (3a)$$

$$u_3(\psi,t)=\sum_{k=2}^{\infty}\eta_k(t)U_{3k}(\psi,t) \quad (3b)$$

where k is the mode number; η_k is the modal participation factor; U_{3k} and $U_{\psi k}$ are, respectively, the kth mode transverse and circumferential mode shape functions; η_k denotes the temporal contribution; and $U_{\psi k}$ and U_{3k} denote the spatial distributions of each mode. When the ring is freely floating in space, it is observed that $k=0$ is a breathing mode; $k=1$ is a rigid body mode, and a set of transverse and circumferential modes occur when $k\geq 2$ [17,20]. The mode shape functions of the circumferential direction and the transverse direction are

$$U_{\psi k}=A_k\sin(k\psi-\varphi) \quad (4a)$$

$$U_{3k}=B_k\cos(k\psi-\varphi) \quad (4b)$$

where A_k and B_k are the modal amplitudes and φ is an arbitrary phase angle indicating an arbitrary ring orientation. Substituting the modal expansions, i.e., Eqs. (3a) and (3b), into ring's governing equations, imposing the orthogonality of the mode shape functions and introducing the modal damping, one derives the independent modal equation [20]

$$\ddot{\eta}_k+2\zeta_k\omega_k\dot{\eta}_k+\omega_k^2\eta_k=\hat{F}_k \quad (5)$$

where ω_k is the kth natural frequency; ζ_k is the modal damping ratio determined by an equivalent damping constant c and the natural frequency ω_k, i.e., $\zeta_k=c/(2\rho h\omega_k)$; and $\hat{F}_k$ is the kth modal force. For each mode of $k\geq 2$, there are two component natural frequencies, i.e., ω_{k1} and ω_{k2}. The component frequency ω_{k1} denotes the transverse vibration, and ω_{k2} denotes the circumferential vibration. Modal vibration amplitudes of the transverse component modes and the circumferential ones are coupled at lower k, i.e., $k\leq 10$, modes. By substituting the mode shape functions into ring's governing equations, the relationship between the modal amplitude A_k of the circumferential mode and that B_k of the transverse mode can be obtained [18,19]. For the oscillation at ω_{k1} and $k\leq 10$, amplitude ratio of transverse modes B_k is proportional to circumferential mode's amplitude A_k as $(B_k/A_k)\approx -k$ [17]. For typical rings, $\omega_{k2}\gg\omega_{k1}$; thus, the circumferential vibration is not considered and only the transverse ω_{k1} remains as ω_k used in the vibration control later.

The modal force can be divided into two components: the modal force induced by the mechanical force $\left(\hat{F}^m_k\right)$ and that induced by the flexoelectric actuator $\left(\hat{F}^a_k\right)$, i.e., $\hat{F}_k=\hat{F}^m_k+\hat{F}^a_k$. Let the transverse external mechanical force be expressed as F_3, see Fig. 1. The modal force components $\hat{F}^m_k$ and $\hat{F}^a_k$ are, respectively, defined as [20]

$$\hat{F}^m_k=\frac{1}{\rho hN_k}\int_0^{2\pi}F_3U_{3k}Rd\psi \quad (6a)$$

$$\hat{F}^a_k=\frac{1}{\rho hN_k}\int_{\psi_1^*}^{\psi_2^*}(L^a_\psi U_{\psi k}+L^a_3U_{3k})Rd\psi \quad (6b)$$

where $N_k=\int_0^{2\pi}(U^2_{\psi k}+U^2_{3k})Rd\psi$. Note that the flexoelectric actuator patch is laminated from ψ_1^* to ψ_2^* on the ring. When the mechanical force F_3 and the actuation voltage ϕ^a are harmonic with the excitation frequency ω, i.e., $F_3=F_3^*e^{j\omega t}$, $\phi^a(t)=\phi^a e^{j\omega t}$, the steady-state modal response is also harmonic and $\hat{F}_k=\hat{F}^*_k e^{j\omega t}$, where $\hat{F}^*_k$ indicates the magnitude of the kth modal force. Solving the modal equation (5) with the modal excitation yields the steady-state modal response

$$\eta_k(t)=\frac{\hat{F}^*_k}{(\omega_k^2-\omega^2)+2j\zeta_k\omega_k\omega}e^{j\omega t}=\frac{\hat{F}^*_k}{\omega_k^2\sqrt{\left(1-\frac{\omega^2}{\omega_k^2}\right)^2+4\zeta_k^2\left(\frac{\omega}{\omega_k}\right)^2}}e^{j(\omega t-\varphi^*)} \quad (7)$$

where ϕ^* is the phase angle expressed as $\varphi^*=\arctan[(2\zeta_k(\omega/\omega_k))/(1-(\omega^2/\omega_k^2))]$. With the modal response Eq. (7) and the mode expansion expression Eq. (3b), the transverse deflection induced by the mechanical force and the flexoelectric actuation becomes

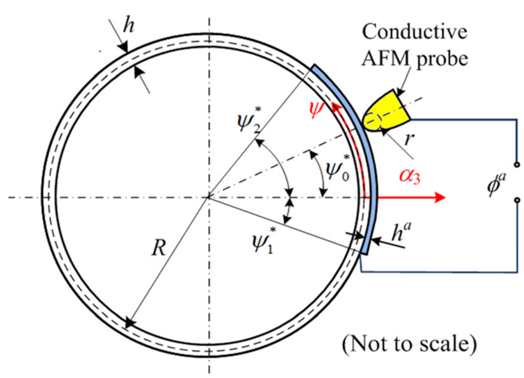

Fig. 2 A ring model of flexoelectric actuation

$$
\begin{aligned}
u_3(\psi,t) &= \sum_{k=2}^{\infty}\eta_k(t)U_{3k}(\psi,t) \\
&= \sum_{k=2}^{\infty}\frac{\hat{F}_k^{\mathrm{m}}+\hat{F}_k^{a}}{\omega_k^2\sqrt{\left(1-\frac{\omega^2}{\omega_k^2}\right)^2+4\zeta_k^2\left(\frac{\omega}{\omega_k}\right)^2}}U_{3k}(\psi,t) \\
&= \sum_{k=2}^{\infty}\frac{U_{3k}(\psi,t)\mathrm{e}^{j(\omega t-\varphi^*)}}{\rho h N_k\omega_k^2\sqrt{\left(1-\frac{\omega^2}{\omega_k^2}\right)+4\zeta_k^2\left(\frac{\omega}{\omega_k}\right)^2}} \\
&\left\{\int_{\psi_1}^{\psi_2}\left[\left(-\frac{1}{R}\frac{\partial N_{\psi\psi}^a}{\partial\psi}-\frac{1}{R^2}\frac{\partial M_{\psi\psi}^a}{\partial\psi}\right)U_{\psi k}\right.\right. \\
&\left.\left.+\left(\frac{N_{\psi\psi}^a}{R}-\frac{1}{R^2}\frac{\partial^2 M_{\psi\psi}^a}{\partial\psi^2}\right)U_{3k}\right]Rd\psi+\int_0^{2\pi}F_3^*U_{3k}Rd\psi\right\}
\end{aligned}
\tag{8}
$$

The transverse vibration of the ring is affected by the flexoelectric membrane control force and the bending control moment. For the flexoelectric material, the actuation behavior depends on the inhomogeneous electric field. Detailed actuation mechanism induced by the flexoelectric patch driven by an AFM-induced electric field is introduced in the Flexoelectric Actuation section.

Flexoelectric Actuation

The ring model with the flexoelectric actuator and an AFM probe is shown in Fig. 2, where r is the AFM probe radius; h^a is the flexoelectric patch thickness; and the flexoelectric patch is laminated from ψ_1^* to ψ_2^* on the ring. According to the *converse flexoelectric effect*, an inhomogeneous electric field is needed to drive the flexoelectric actuator patch and this electric field is induced by an AFM probe located at $\psi=\psi_0^*$. The AFM probe tip radius r is far less than the flexoelectric patch thickness and the patch thickness is far less than the ring thickness, i.e., $r \ll h^a \ll h$.

To generate the inhomogeneous electric field, an actuation voltage ϕ^a is applied between the AFM probe and the bottom surface electrode of the flexoelectric patch. The electric potential ϕ inside the flexoelectric patch can be expressed based on Abplanalp's approximate [21]. Transforming the rectangular coordinates to the polar coordinates yields the potential near the AFM probe

$$
\phi = \frac{\phi^a r}{\sqrt{(\alpha_3+R)^2\sin^2(\psi-\psi_0^*)+\left[r+\frac{h}{2}+h^a-(\alpha_3+R)\cos(\psi-\psi_0^*)+R^2\right]}} \tag{9}
$$

where ψ_0^* is the AFM probe location. In this study, the net electric field in the ψ direction is almost zero [16]; thus, only the transverse electric field is considered here. The transverse electric field E_3 can be obtained by differentiating the potential in the transverse direction.

$$
\begin{aligned}
E_3 = -\frac{\partial\phi}{\partial\alpha_3} &= \phi^a r\left\{(R+\alpha_3)\sin^2(\psi-\psi_0^*)-\left[r+\frac{h}{2}+h^a-(R+\alpha_3)\cos(\psi-\psi_0^*)+R\right]\cos(\psi-\psi_0^*)\right\} \\
&\times\left\{(R+\alpha_3)^2\sin^2(\psi-\psi_0^*)+\left[r+\frac{h}{2}+h^a-(R+\alpha_3)\cos(\psi-\psi_0^*)+R\right]^2\right\}^{-\frac{3}{2}}
\end{aligned}
\tag{10}
$$

Note that this electric field denotes the field near the AFM probe. For the area away from the AFM probe, the electric field is nearly zero [10,16]. The circumferential stress induced by the electric field can be defined from the converse flexoelectric equation [16]

$$
\begin{aligned}
T_{\psi\psi}^a = \pi_{12}\frac{\partial E_3}{\partial\alpha_3} &= \frac{\pi_{12}\phi^a r}{\left\{(R+\alpha_3)^2\sin^2(\psi-\psi_0^*)+\left[r+\frac{h}{2}+h^a-(R+\alpha_3)\cos(\psi-\psi_0^*)+R\right]^2\right\}^{\frac{3}{2}}} \\
&-\frac{\frac{3}{2}\pi_{12}\phi^a r}{\left\{(R+\alpha_3)^2\sin^2(\psi-\psi_0^*)+\left[r+\frac{h}{2}+h^a-(R+\alpha_3)\cos(\psi-\psi_0^*)+R\right]^2\right\}^{\frac{5}{2}}} \\
&\times\left\{(R+\alpha_3)\sin^2(\psi-\psi_0^*)-\left[r+\frac{h}{2}+h^a-(R+\alpha_3)\cos(\psi-\psi_0^*)+R\right]\cos(\psi-\psi_0^*)\right\} \\
&\times\left\{2(R+\alpha_3)\sin^2(\psi-\psi_0^*)-2\left[r+\frac{h}{2}+h^a-(R+\alpha_3)\cos(\psi-\psi_0^*)+R\right]\cos(\psi-\psi_0^*)\right\}
\end{aligned}
\tag{11}
$$

where $T_{\psi\psi}^a$ denotes the circumferential stress in the flexoelectric actuator patch. The flexoelectric membrane control force induced by the electric field is obtained by integrating the stress along the actuator thickness

Table 1 Parameters and properties of the ring model

Properties	Values
Ring radius, R (m)	0.05
Ring width, b (m)	0.010
Ring thickness, h (m)	0.001
Young's modulus of ring, Y (N/m^2)	1.556×10^9
Flexoelectric patch thickness, h^a (μm)	50
AFM probe tip radius, r (nm)	50
AFM probe tip location, ψ_0^* (rad)	0
Ring mass density, ρ (kg/m^3)	1100
Poisson's ratio, μ	0.3
Flexoelectric constant, π_{12} (μC/m)	100
Actuator voltage, ϕ^a (V)	1
Starting position of patch, ψ_1^* (rad)	$-\pi/40$
Ending position of patch, ψ_2^* (rad)	$\pi/40$

$$N_{\psi\psi}^a = \int_{\frac{h}{2}}^{\frac{h}{2}+h^a} T_{\psi\psi}^a d\alpha_3 \quad (12)$$

The flexoelectric control moment is calculated by integrating the product of the actuation stress and the corresponding moment arm (the distance between the local point and ring's neutral layer) as

$$M_{\psi\psi}^a = \int_{\frac{h}{2}}^{\frac{h}{2}+h^a} \alpha_3 T_{\psi\psi}^a d\alpha_3 \quad (13)$$

With the explicit expressions of the membrane control force and bending control moment induced by the flexoelectric actuator, microscopic actuation behaviors and the flexoelectric actuation responses with respect to various design parameters can be evaluated in the Parameter Studies section.

Flexoelectric Actuation Mechanism and Vibration Control

With the geometric and material parameters listed in Table 1, microscopic actuation behavior of the flexoelectric patch and the modal control effects of the ring shell with various design parameters are evaluated in this section. Since the converse flexoelectric effect depends on the electric field gradient, this gradient is analyzed first, followed by a detailed evaluation of the flexoelectric membrane control force and control moments. Steady-state maximal controllable displacements for various ring modes are analyzed with respect to actuator thickness, AFM probe radius, ring thickness, and radius when the actuation voltage ϕ^a is set at a unit voltage (since the actuation effect is proportional to the magnitude of actuation voltage). Numerical calculations are implemented in MAPLE software and verified by the TRAPZ integration method in MATLAB.

Distribution of the Transverse Electric Field. With the parameters in Table 1, the transverse distribution of the electric field gradient defined in Eqs. (9) and (10) is analyzed first. By the flexoelectric stress equation, i.e., Eq. (11), the induced stress in the flexoelectric actuator is proportional to the gradient of the transverse electric field. Figure 3 shows the electric field gradient variation in the transverse direction underneath the AFM contact point. Note that the vertical coordinate is set to start on the top surface of the flexoelectric patch and points downward to the bottom surface, i.e., from 0 to 50, 75, and 100 μm.

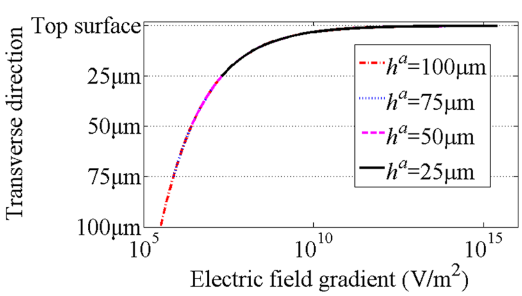

Fig. 3 The transverse distribution of the electric field gradient

Figure 3 reveals that the electric field gradient is extremely high at the AFM probe contact point (or thickness equals to zero). The gradient in the lower part of the patch is relatively small as compared with that of the upper surface. For example, the magnitude of the electric gradient at the half thickness of the patch (thickness equal to 25 μm) is only 7.92×10^{-7}% of the top surface (thickness equal to zero). Equation (11) shows that the induced stress $T_{\psi\psi}^a$ is proportional to the electric field gradient; thus, the stress on the upper part of the flexoelectric patch is much larger than the lower part, indicating that the upper part is a dominant component of the induced membrane control force $N_{\psi\psi}^a$. Further analysis indicates that the gradient distribution of various actuator thicknesses is similar. The top portions of various actuator thicknesses near the AMF probe are the same and the distribution follows the same trend extending down as the actuator becomes thicker, i.e., 50, 75, and 100 μm. The membrane force induced by the upper part of the patch dominates the overall flexoelectric membrane control force. Hence, the actuation effect increases little as the patch thickens and this behavior is further validated later.

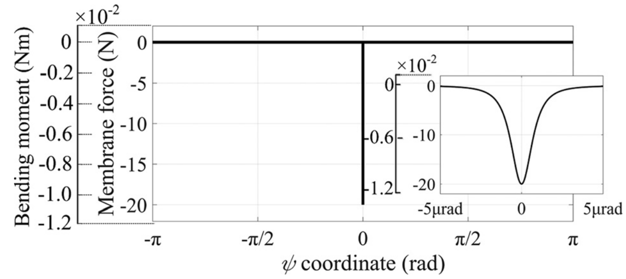

Fig. 4 Circumferential distribution of the actuation

Microscopic Flexoelectric Actuation Behavior. Microscopic actuation behavior of the flexoelectric patch is investigated here. Due to the sharpness of the AFM probe-induced electric field gradient, the circumferential distributions of the membrane force is like a spike, i.e., Dirac delta function. Figure 4 shows the circumferential distribution (i.e., from $-\pi$ to $+\pi$ of the ring with the AFM probe placed at $\psi_0^* = 0$) of the induced flexoelectric membrane force and control moment, respectively, marked on different scales.

Figure 4 indicates that the spatial distribution of the membrane force is extremely inhomogeneous. Note that the insert picture in Fig. 4 illustrates the force distribution in a very small region, i.e., from -5×10^{-6} rad to 5×10^{-6} rad, which illustrates that the

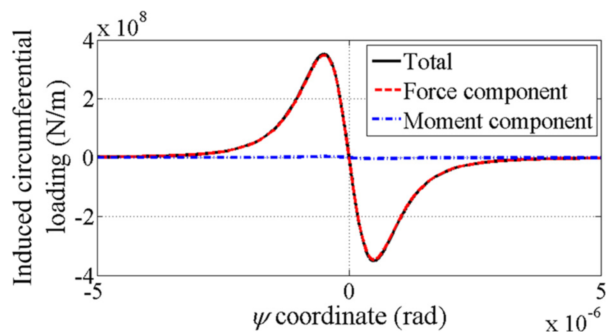

Fig. 5 The distribution of the circumferential loading induced by actuator

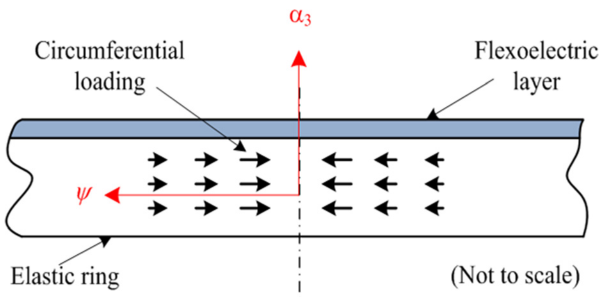

Fig. 6 Distribution of the induced circumferential loading

membrane force concentrates near the AFM location. The circumferential distribution of bending moment is also observed in Fig. 4 with the moment scale on the left. The moment arm is constant in the ring model; thus, the control moment is proportional to the membrane control force and its distribution is similar. The actuation effect, as indicated by the insert picture in Fig. 4, is limited in a very small region, specifically, around 0.5 μm. The following analysis focuses on this microscopic region and evaluates its detailed microscopic actuation characteristic.

As discussed previously, the Love control operator in the total flexoelectric actuation, i.e., $\hat{F}_k^a = (1/(\rho h N_k)) \int_{\psi_1}^{\psi_2} (L_\psi^a U_{\psi k} + L_3^a U_{3k}) R d\psi$ in Eq. (6*b*), has two actuation terms: the circumferential component L_ψ^a and the transverse component L_3^a and these two components are, respectively, investigated to evaluate the flexoelectric microscopic actuation behavior near the AMF actuation point. Comparing Eq. (6*a*) with Eq. (6*b*), the transverse Love operator L_3^a can be regarded as the transverse loading and the circumferential Love operator L_ψ^a be the circumferential loading induced by the flexoelectric actuator. The characteristics of these two induced loadings or control actions are, respectively, analyzed next.

Flexoelectric Circumferential Actuation. As discussed earlier, L_ψ^a has two components: one is induced by the flexoelectric membrane force and the other by the bending control moment. The circumferential distributions of these two components and their total effect are shown in Fig. 5.

Figure 5 reveals that in the region on the left of the $\psi = 0$, the circumferential loading points rightward and that on the right points leftward. In another word, the circumferential actuation points to the AFM probe contact location. Figure 5 also shows that the membrane force component dominates the total induced circumferential actuation. This result is reasonable because the membrane force mainly influences the circumferential vibrations, while the bending moment mainly influences the transverse ones. The induced microscopic circumferential actuation behavior is shown in Fig. 6. The appearance of the AFM probe's electric field results in a circumferential control actuation draging the material to where the probe locates.

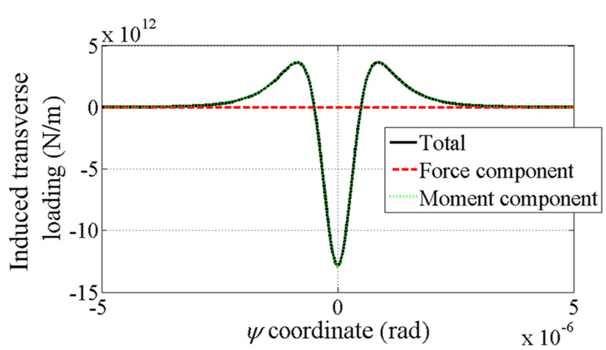

Fig. 7 The distribution of the transverse loading induced by actuator

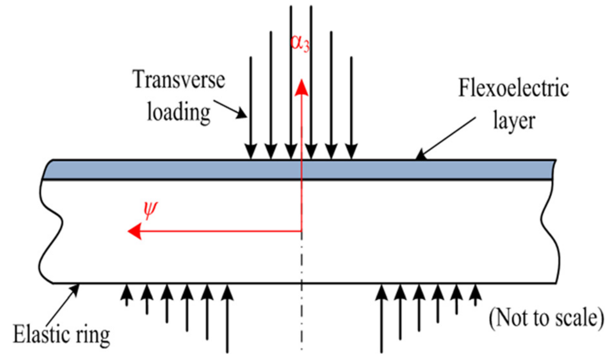

Fig. 8 Distribution of the induced transverse loading

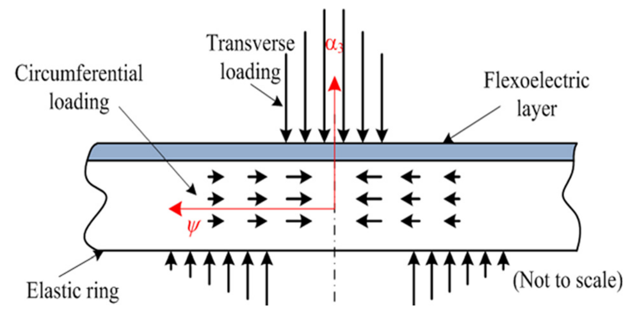

Fig. 9 Circumferential distribution of the total induced flexoelectric actuation near the AFM probe

Flexoelectric Transverse Actuation. The transverse oscillation is mainly influened by the actuator-induced transverse Love operator L_3^a when the transverse mechanical input $L_3^m = 0$. The distribution of the two transverse flexoelectric actuation components, i.e., the membrane force component and control moment component, together with their total effect, are plotted in Fig. 7. As shown in Fig. 7, the induced actuation is downward in the region closed to the AFM probe; the actuation is upward in the region away from the AFM probe and the region farther away is almost zero.

Detailed microscopic transverse actuation behavior is shown in Fig. 8. The bending control moment plays a dominant role in the transverse actuation, because the transverse deformation can be considered as a drastic "folding" resembling a Dirac delta function at the AFM probe's contact point, see Fig. 8. Note that this sharp bending has been described as the buckling characteristic in an earlier research on static deformation control of the cantilever beam based on an AFM probe [16].

To analyze the characteristic of the flexoelectric patch under the AFM control, L_ψ^a and L_3^a should be considered as a whole. The

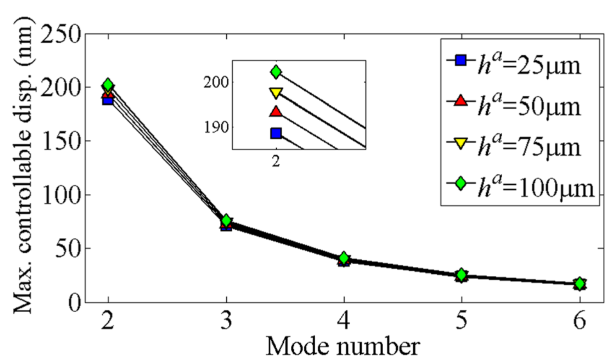

Fig. 10 Maximal controllable displacement ($k = 2$–6 ring modes) with flexoelectric patch thickness

schematic diagram of the total distributed flexoelectric actuation on the ring is shown in Fig. 9.

When the ring is actuated by the flexoelectric actuator driven by an AFM probe, a transverse deformation is induced as illustrated above. As the deformation occurs, the material is dragged to where the AFM probe locates, while the ring would resist such drag and results in a circumferential actuation. Thus, the overall actuation effect of the flexoelectric patch on the ring can be regarded as a drastic sharp bending effect within a small region. Steady-state dynamic responses and controllable displacements of the ring actuated by a flexoelectric actuator with various design parameters are analyzed next.

Parameter Studies. The microscopic behavior of the flexoelectric actuator indicates that the actuation only exists in a very small region, i.e., near the AFM contact point. Thus, the patch size has little influence on the overall actuation effect. A relatively small patch, covers from $-\pi/40$ to $\pi/40$, is chosen for the displacement control of rings. Other material and geometric properties are summarized in Table 1. To further evaluate the actuation effect, dynamic responses and controllable displacements of the elastic ring with a flexoelectric actuator are analyzed with respect to design parameters, e.g., the flexoelectric patch thickness, AFM probe radius, ring thickness, and ring radius here.

Flexoelectric Patch Thickness. The influence of flexoelectric patch thickness on control of ring oscillations is analyzed first. The flexoelectric-induced oscillation amplitudes (or the maximal controllable displacements) driven by a steady-state unit voltage are used to compensate ring's vibration amplitudes, i.e., the larger the actuator-induced magnitudes, the better the vibration control effects on rings. The maximal flexoelectric-induced displacements of $k=2$–6 modes are evaluated with respect to patch thickness of 25 μm, 50 μm, 75 μm, and 100 μm in Fig. 10. (Recall that $k=1$ is a rigid-body ring mode.) Note that steady-state controllable displacements of 2–6 modes are calculated when the actuation frequency is, respectively, set to its natural frequency.

Figure 10 shows that when the actuator thickness increases, the maximal induced displacement of $k=2$–6 increases. The membrane control force in the flexoelectric patch is enhanced as the patch thickness increases. Furthermore, the induced control moment is enhanced because the moment arm increases as the flexoelectric actuator thickens.

Atomic Force Microscope Probe Radius. Earlier analysis indicates that the AFM probe radius is a key factor influencing the electric field gradient, membrane control force, and control moments, consequently the vibration control effectiveness. The influence of the AFM probe radius on the actuation effect is evaluated here. The maximal controllable displacement of $k=2$–6 ring modes are evaluated with respect to probe radius of 25 nm, 50 nm, 75 nm, and 100 nm in Fig. 11.

As shown in Fig. 11, the maximal displacement decreases as the radius of AFM probe increases from 25 nm to 100 nm.

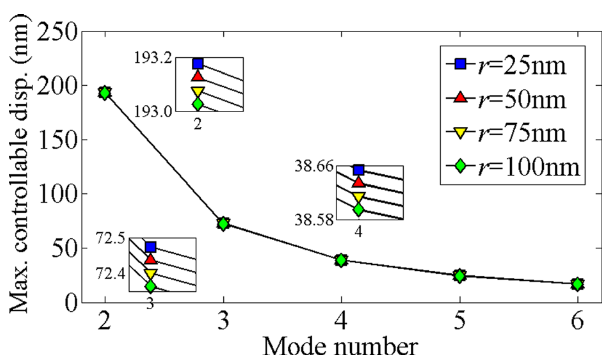

Fig. 11 Maximal controllable displacement ($k=2$–6 ring modes) with the radius of AFM probe

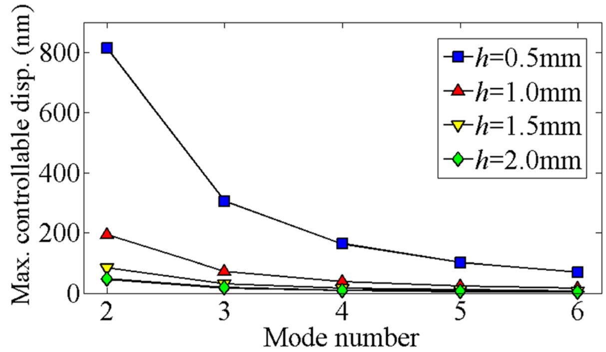

Fig. 12 Maximal controllable displacement ($k=2$–6 ring modes) with the ring thickness

Although the circumferential domain of the electric field grows with probe radius, the maximal electric field gradient decreases, which leads to the decrease of the maximal membrane force in the flexoelectric actuator. The latter decrease outweighs the former increases, as a result the actuation effect decreases as the AFM probe radius increases from 25 nm to 100 nm.

Ring Thickness. After analyzing flexoelectric actuator characteristics (e.g., the AFM probe and the flexoelectric patch), the influence of the structural characteristics of the elastic ring is also evaluated here. The maximal controllable displacements of $k=2$–6 modes are calculated with respect to ring thickness of 0.5 mm, 1.0 mm, 1.5 mm, and 2.0 mm in Fig. 12.

As shown in Fig. 12, the maximal ring displacement increases as the ring thickness decreases. Keeping other parameters unchanged, it is obvious that as a thicker ring becomes stiffer resulting in higher natural frequencies. For a specific ring mode, Fig. 12 shows that the relationship between the maximal controllable displacement and ring thickness is quadric. The bending stiffness is proportional to the cubic of ring thickness and the induced bending moment is proportional to the ring thickness. Thus, the actuation effect, which is contributed by both factors, is proportional to the square of ring thickness.

Ring Radius. The influence of ring radius on the actuation effect is also evaluated. Maximal controllable displacements of modes 2–6 with respect to ring radius of 25 mm, 50 mm, 75 mm, and 100 mm are plotted in Fig. 13.

Figure 13 indicates that the maximal displacement for each mode increases with the ring radius. With other parameters and dimensions fixed, a ring with larger radius is softer than a smaller radius one. Furthermore, as the ring radius increases, the natural frequency decreases, and thus, the ring become relatively easier to actuate and control. The maximal controllable displacement, for each mode, respectively, is proportional to the ring radius as plotted in Fig. 13. For two rings with different radius, they share the

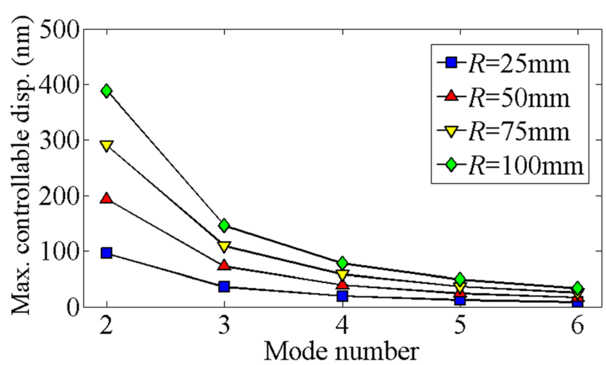

Fig. 13 Maximal controllable displacement ($k=2$–6 ring modes) with the ring radius

same bending stiffness and actuation force. Thus, it is reasonable to deduce that the relationship between actuation effect and the ring size is linear.

Conclusions

This study focused on the converse flexoelectricity-based dynamic actuation characteristics and vibration control of elastic rings. The *converse flexoelectric effect*-induced actuation depends on an inhomogeneous electric filed implemented by an AFM probe on a flexoelectric actuator patch. The distribution of the induced stress in the flexoelectric actuator patch is extremely nonuniform. The top surface induces the majority of the induced membrane control force. Furthermore, the transverse distribution of the electric gradient does not change with the actuator thickness. In the circumferential direction, the distribution of actuation forces resembles a Dirac delta function due to the inhomogeneous electric field gradient induced by the AFM probe. The microscopic behaviors of induced circumferential and transverse control actions were evaluated, and the flexoelectric actuations were applied to actuate a ring. With the basic dynamics of elastic rings, flexoelectric vibration characteristics were studied and the maximal controllable displacements for five ring modes, i.e., $k = 2$–6, were evaluated with respect to the actuator patch (thickness), the AFM probe (tip radius), and the ring (thickness and radius). The actuation effect is enhanced with a thicker flexoelectric actuator, a smaller AFM probe radius, thinner ring shell, or larger ring radius.

Accordingly, this study provides a basic understanding of the microscopic flexoelectric actuation behavior, including: (1) the nonuniform distribution of actuation stress in the transverse direction and actuation forces in the circumferential direction and (2) the equivalent action loadings and the drastic buckling induced by the flexoelectric actuator. The analysis of flexoelectric actuator's microscopic behavior is not confined to ring structures. It serves as a foundation for the flexoelectricity-based actuation and vibration control of other shell and nonshell structures.

Acknowledgment

This work was supported by the National Natural Science Foundation of China (Nos. 11472241 and 11321202) and the Nanjing University of Aeronautics and Astronautics (NUAA-NP2016203 and NUAA-MCMS-0516G01).

Nomenclature

A_k = constant in circumferential mode shape function
b = ring width
B_k = constant in transverse mode shape function
c = equivalent damping constant
E_3 = electric field strength in transverse direction
F_3 = transverse mechanical force
$\hat{F}_k$ = modal force
$\hat{F}_k^a$ = actuator-induced modal force
$\hat{F}_k^m$ = mechanical force-induced modal force
$\hat{F}_k^*$ = magnitude of modal force
F_3^* = magnitude of transverse mechanical force
h = ring thickness
h^a = flexoelectric patch thickness
k = mode number
L_3^a = transverse love's operator
L_ψ^a = circumferential love's operator
$M_{\psi\psi}^a$ = actuator-induced circumferential bending moment
$N_{\psi\psi}^a$ = actuator-induced circumferential membrane force
r = AFM probe radius
R = ring radius
$T_{\psi\psi}^a$ = actuator-induced circumferential stress
u_3 = transverse displacement of ring
U_{3k} = transverse mode shape function
$U_{\psi k}$ = circumferential mode shape function
Z_k = modal damping ratio
α_3 = transverse coordinate
η_k = modal participation factor
ρ = ring density
ϕ = potential field
ϕ^a = actuation voltage
φ^* = lagging phase angle
ψ = circumferential coordinate
ψ_0^* = AFM probe tip location
ψ_1^* = starting position of flexoelectric patch
ψ_2^* = ending position of flexoelectric patch
ω = excitation frequency
ω_k = natural frequency of ring

References

[1] Kogan, S. M., 1964, "Piezoelectric Effect During Inhomogeneous Deformation and Acoustic Scattering of Carriers in Crystals," Sov. Phys. Solid State, **5**(10), pp. 2069–2070.
[2] Tagantsev, A. K., 1986, "Piezoelectricity and Flexoelectricity in Crystalline Dielectrics," Phys. Rev. B, **34**(8), pp. 5883–5889.
[3] Todorov, A. T., Petrov, A. G., and Fendler, J. H., 1994, "First Observation of the Converse Flexoelectric Effect in Bilayer Lipid Membranes," J. Chem. Phys., **98**(12), pp. 3076–3079.
[4] Mindlin, R. D., 1969, "Continuum and Lattice Theories of Influence of Electromechanical Coupling on Capacitance of Thin Dielectric Films," Int. J. Solids Struct., **5**(11), pp. 1197–1208.
[5] Mindlin, R. D., and Eshel, N. N., 1968, "On First Strain-Gradient Theories in Linear Elasticity," Int. J. Solids Struct., **4**(1), pp. 109–124.
[6] Sahin, E., and Dost, S., 1988, "A Strain-Gradients Theory of Elastic Dielectrics With Spatial-Dispersion," Int. J. Eng. Sci., **26**(12), pp. 1231–1245.
[7] Cross, L. E., 2006, "Flexoelectric Effects: Charge Separation in Insulating Solids Subjected to Elastic Strain Gradients," J. Mater. Sci., **41**(1), pp. 53–63.
[8] Baskaran, S., He, X., and Chen, Q., 2011, "Experimental Studies on the Direct Flexoelectric Effect in α-Phase Polyvinylidene Fluoride Films," Appl. Phys. Lett., **98**(24), p. 242901.
[9] Fu, J. Y., Zhu, W., Li, N., and Cross, L. E., 2006, "Experimental Studies of the Converse Flexoelectric Effect Induced by Inhomogeneous Electric Field in a Barium Strontium Titanate Composition," J. Appl. Phys., **100**(2), p. 024112.
[10] Agronin, A., Molotskii, M., Rosenwaks, Y., Rosenman, G., Rodriguez, B. J., Kigon, A. I., and Gruverman, A., 2006, "Dynamics of Ferroelectric Domain Growth in the Field of Atomic Force Microscope," J. Appl. Phys., **99**(10), p. 104102.
[11] Zubko, P., Catalan, G., Buckley, A., Welche, P. R. L., and Scott, J. F., 2007, "Strain-Gradient-Induced Polarization in $SrTiO_3$ Single Crystals," Phys. Rev. Lett., **99**(16), p. 167601.
[12] Hu, S. D., Li, H., and Tzou, H. S., 2013, "Flexoelectric Responses of Circular Rings," ASME J. Vib. Acoust., **135**(2), p. 021003.
[13] Rao, Z., Hu, S. D., and Tzou, H. S., 2011, "Diagonal Flexoelectric Sensor on Cylindrical Shell Substructure," Symposium on Piezoelectricity, Acoustic Waves, and Device Applications (SPAWDA), Shenzhen, China, Dec. 9–11, pp. 106–111.
[14] Tzou, H. S., and Zhang, X. F., 2016, "A Flexoelectric Double-Curvature Nonlinear Shell Energy Harvester," ASME J. Vib. Acoust., **138**(2), p. 031006.
[15] Hu, S. D., Li, H., and Tzou, H. S., 2014, "Comparison of Flexoelectric and Piezoelectric Dynamic Signal Responses on Flexible Rings," J. Intell. Mater. Syst. Struct., **25**(7), pp. 832–844.
[16] Hu, S. D., Li, H., and Tzou, H. S., 2011, "Static Nano-Control of Cantilever Beams Using the Inverse Flexoelectric Effect," ASME Paper No. IMECE2011-65123.
[17] Soedel, W., 1993, *Vibrations of Shells and Plates*, Marcel Dekker, New York.
[18] Tzou, H. S., Zhong, J. P., and Natori, M. C., 1993, "Sensor Mechanics of Distributed Shell Convolving Sensors Applied to Flexible Rings," ASME J. Vib. Acoust., **115**(1), pp. 40–46.
[19] Tzou, H. S., Zhong, J. P., and Hollkamp, J. J., 1994, "Spatially Distributed Orthogonal Piezoelectric Shell Actuators: Theory and Applications," J. Sound Vib., **177**(3), pp. 363–378.
[20] Tzou, H. S., 1993, *Piezoelectric Shells: Distributed Sensing & Control of Continua*, Kluwer Academic Publishers, Dordrecht, The Netherlands.
[21] Abplanalp, M., 2001, "Piezoresponse Scanning Force Microscopy of Ferroelectric Domains," Ph.D. dissertation, Swiss Federal Institute of Technology, Zürich, Switzerland.